

# Averting H<sup>+</sup>-Mediated Charge Storage Chemistry Stabilizes the High Output Voltage of LiMn<sub>2</sub>O<sub>4</sub>-Based Aqueous Battery

Abhirup Bhadra, S. Swathilakshmi, Uttam Mittal, Neeraj Sharma,\* Gopalakrishnan Sai Gautam,\* and Dipan Kundu\*

H<sup>+</sup> co-intercalation chemistry of the cathode is perceived to have damaging consequences on the low-rate and long-term cycling of aqueous zinc batteries, which is a critical hindrance to their promise for stationary storage applications. Herein, the thermodynamically competitive H<sup>+</sup> storage chemistry of an attractive high-voltage cathode LiMn<sub>2</sub>O<sub>4</sub> is revealed by employing *operando* and ex-situ analytical techniques together with density functional theory-based calculations. The H<sup>+</sup> electrochemistry leads to the previously unforeseen voltage decay with cycling, impacting the available energy density, particularly at lower currents. Based on an in-depth investigation of the effect of the Li<sup>+</sup> to Zn<sup>2+</sup> ratio in the electrolyte on the charge storage mechanism, a purely aqueous and low-salt concentration electrolyte with a tuned Li<sup>+</sup>/Zn<sup>2+</sup> ratio is introduced to subdue the H<sup>+</sup>-mediated charge storage kinetically, resulting in a stable voltage output and improved cycling stability at both low and high cathode loadings. Synchrotron X-ray diffraction analysis reveals that repeated H<sup>+</sup> intercalation triggers an irreversible phase transformation leading to voltage decay, which is averted by shutting down H<sup>+</sup> storage. These findings unveiling the origin and impact of the deleterious H<sup>+</sup>-storage, coupled with the practical strategy for its inhibition, will inspire further work toward this under-explored realm of aqueous battery chemistry.

electrochemical storage options,<sup>[3]</sup> but a few combine low cost, safety, sustainability, recyclability, and competitive energy and power densities. Aqueous zinc batteries (AZBs) can potentially fulfill most of these requirements,<sup>[4–6]</sup> and those with manganese oxide-based cathodes are particularly promising owing to their high voltage and attractive specific capacities aside from the resource abundance of manganese.  $\alpha$ -MnO<sub>2</sub> and spinel-LiMn<sub>2</sub>O<sub>4</sub> are two prime candidates<sup>[7,8]</sup> that, under practically relevant cell conditions, can deliver energy densities exceeding 85 Wh kg<sup>-1</sup> and push beyond 100 Wh kg<sup>-1</sup> if commercial Li-ion cell conditions can be mimicked in AZBs due to the use of energy-dense zinc metal anode.<sup>[9]</sup> Yet, the scalability of their performance with increasing cathode loading and durability under low current densities remains a critical concern for scalable development.<sup>[10]</sup>

The stability issues for oxide cathodes – especially at low current rates – have often been linked to the charge storage mechanism, including active material

dissolution and dominant proton (H<sup>+</sup>) intercalation.<sup>[11–15]</sup> The latter leads to the accumulation of electrically and ionically insulating layered double hydroxide (LDH) byproducts, for example, Zn<sub>n</sub>SO<sub>4</sub>(OH)<sub>6</sub>·nH<sub>2</sub>O (ZHS), formed by the reaction of OH<sup>-</sup> (left behind after H<sup>+</sup> intercalation) with Zn<sup>2+</sup> and SO<sub>4</sub><sup>2-</sup> in the aqueous zinc sulfate electrolyte,<sup>[12,16,17]</sup> on the cathode during discharge and the ZHS dissolution through reaction with egressed

## 1. Introduction

For optimal energy storage and distribution across the renewable energy landscape, it is necessary to develop a portfolio of storage solutions considering their strengths and limitations and the requirements of the applications and deployment environment.<sup>[1,2]</sup> There are many alternatives to Li-ion batteries among

A. Bhadra, D. Kundu  
School of Chemical Engineering  
UNSW Sydney  
Kensington, NSW 2052, Australia  
E-mail: [dkundu@unsw.edu.au](mailto:dkundu@unsw.edu.au)

S. Swathilakshmi, G. Sai Gautam  
Department of Materials Engineering  
Indian Institute of Science  
Bengaluru 560012, India  
E-mail: [saigautamg@iisc.ac.in](mailto:saigautamg@iisc.ac.in)

U. Mittal, N. Sharma  
School of Chemistry  
UNSW Sydney  
Kensington, NSW 2052, Australia  
E-mail: [neeraj.sharma@unsw.edu.au](mailto:neeraj.sharma@unsw.edu.au)

D. Kundu  
School of Mechanical and Manufacturing Engineering  
UNSW Sydney  
Kensington, NSW 2052, Australia

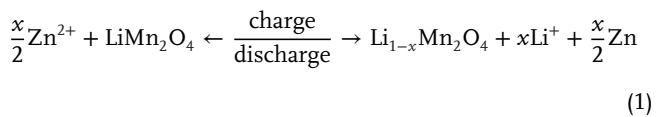
 The ORCID identification number(s) for the author(s) of this article can be found under <https://doi.org/10.1002/smtd.202400070>

© 2024 The Authors. Small Methods published by Wiley-VCH GmbH. This is an open access article under the terms of the [Creative Commons Attribution-NonCommercial License](#), which permits use, distribution and reproduction in any medium, provided the original work is properly cited and is not used for commercial purposes.

DOI: [10.1002/smtd.202400070](https://doi.org/10.1002/smtd.202400070)

$H^+$  during charge. The insulating ZHS may not only add to the polarization losses but also limit charge transport across the interface at a large extent of coverage and lead to reversibility challenges due to their detachment from the cathode surface and inability to combine with emerging  $H^+$ .<sup>[12,18]</sup> Not to mention, these problems will intensify at high cathode loadings. The  $H^+$  intercalation may also lead to irreversible structural degradation<sup>[19]</sup> and irreversible capacity and/or voltage decay. Notwithstanding, the detrimental consequence of  $H^+$  co-intercalation from mildly acidic aqueous electrolytes in AZBs has received limited attention so far, and the only solution seems to be the suppression of water (and thus  $H^+$ ) activity through an extremely high concentration of salts (i.e., water-in-salt type electrolytes) or addition of a large mass/volume fraction (>50%) of nonaqueous solvents.<sup>[18,20–23]</sup> While these approaches overcome the  $H^+$ -mediated charge storage and the associated deleterious effect, they compromise the low-cost and safety advantage of AZBs and sacrifice other properties like small polarization losses and fast kinetics that are conducive to better energy and power densities. Thus, improving the fundamental understanding of the mechanisms involved in  $H^+$  co-intercalation is essential to devise strategies to mitigate it without compromising the advantages of aqueous systems.

$LiMn_2O_4$  is an attractive high-voltage cathode material with a median discharge voltage of  $\approx 1.8$  V in hybrid AZBs employing a  $Li^+/Zn^{2+}$  dual ion electrolyte.<sup>[23,24]</sup> Thanks to the high operating voltage, this hybrid battery can deliver a high energy density of over 100 Wh kg<sup>-1</sup>, under commercially relevant parameters,<sup>[9]</sup> and a high power density owing to fast  $Li^+$  diffusion kinetics.<sup>[25]</sup> Yan et al. first proposed a  $LiMn_2O_4$ -Zn-based rechargeable hybrid aqueous battery,<sup>[26]</sup> where they offered  $Li^+$  (de)intercalation mediated charge storage for  $LiMn_2O_4$  coupled zinc deposition/dissolution at the anode (Figure S1, Supporting Information), and the mechanism can be expressed as below.



Performance degradation in aqueous  $LiMn_2O_4$  system has typically been associated with strong Jahn–Teller distortion of  $Mn^{3+}$  that facilitates its disproportionation to  $Mn^{4+}$  and  $Mn^{2+}$  and concomitant  $Mn^{2+}$  dissolution<sup>[27,28]</sup> aside from surface degradation through reaction with water/oxygen.<sup>[25]</sup> Quite interestingly, the charge storage mechanism of  $LiMn_2O_4$  in aqueous electrolytes had never been directly probed, and the assumption about exclusive  $Li^+$  intercalation remains speculative. Despite the recurrent  $H^+$  intercalation narrative among oxide and polyanionic cathodes in AZBs, it has not been suspected for  $LiMn_2O_4$  thus far.

In this context, here, for the first time, an in-depth investigation of the  $LiMn_2O_4$  charge storage mechanism in aqueous sulfate electrolyte is presented, and  $H^+$  co-intercalation with  $Li^+$  is unveiled to be the operating mechanism that leads to continuous voltage decay. The effect of the  $Li^+$  to  $Zn^{2+}$  concentration ratio in the electrolyte on the charge storage mechanism is thoroughly probed by *operando* X-ray diffraction (XRD) and quantitatively evaluated. Based on this analysis, a purely aqueous electrolyte with tuned  $Li^+/Zn^{2+}$  concentration is shown to effectively shut down the detrimental  $H^+$ -mediated charge stor-

age in  $LiMn_2O_4$ , resulting in stable voltage (1.8 V vs. Zn) output and improved cycling stability at both low and high cathode loading. Density functional theory (DFT)<sup>[29,30]</sup> based calculations reveal that while  $Li^+$  and  $H^+$  intercalation processes can occur at similar voltages against the standard hydrogen electrode (SHE) reference ( $\approx 1.30$ – $1.38$  V for  $H^+$ ;  $\approx 1.55$  V for  $Li^+$ ),  $Zn^{2+}$  intercalation occurs at a significantly different voltage ( $\approx 0.85$  V vs SHE or  $\approx 1.62$  V vs Zn), which highlights the propensity of  $Li^+$ - $H^+$  co-intercalation to occur in typical aqueous electrolytes. Additionally, an irreversible phase transformation induced by  $H^+$  storage is unveiled using synchrotron XRD-assisted postmortem analysis of the cycled electrode, which is significantly suppressed in the optimized electrolyte. Thus, our work should aid in the design of optimal aqueous electrolytes that can substantially suppress detrimental  $H^+$  co-intercalation and improve the reversibility and practical deployability of AZBs.

## 2. Results and Discussion

### 2.1. $H^+$ Co-Intercalation Chemistry and Its Consequence for the $LiMn_2O_4$ Cathode in AZBs

The as-purchased  $LiMn_2O_4$  was analyzed by X-ray diffraction (XRD) and electron microscopy to confirm the phase purity and particle size of the material. Figure 1a shows Rietveld's analysis of the structural model using the laboratory powder XRD data, revealing a refined lattice parameter of  $8.235(9)\text{\AA}$  for the cubic spinel ( $Fd\bar{3}mZ$ )  $LiMn_2O_4$ . Synchrotron XRD data provides a similarly good fit (Figure S1, Supporting Information), featuring exclusively the spinel  $LiMn_2O_4$ . A representative field-emission scanning electron microscopy (FE-SEM) image of the material, as shown in Figure 1b, reveals somewhat deformed cubic morphology and relatively uniform size distribution with an average particle size of  $\sim 50$ – $100$  nm. The scanning transmission electron microscopy (STEM) image of a single  $LiMn_2O_4$  particle (Figure 1c) further confirms the SEM observation, and the corresponding energy dispersive X-ray spectroscopy (EDX) mapping (Figure 1d) highlights the uniform distribution of Mn in the particle.

The charge storage mechanism of  $LiMn_2O_4$  with  $1\text{ M }Li_2SO_4$  –  $1\text{ M }ZnSO_4$  in water (referred to as the 1-1 electrolyte here), which is the standard electrolyte solution employed in  $LiMn_2O_4$  based dual-ion or hybrid AZBs,<sup>[24]</sup> was probed by *operando* XRD. The 2D contour profile in Figure 2a–d displays the  $LiMn_2O_4$  phase evolution during the first charge-discharge cycle. The shift in characteristic diffraction peaks denoting (111) and (400) planes of spinel  $LiMn_2O_4$  (Figure 2c,d) represents the volume expansion – contraction associated with the cation ( $Li^+/H^+/Zn^{2+}$ ) deintercalation – intercalation. Cations screen the electrostatic repulsion between the oxide anions in the lattice, and thus, their intercalation leads to the shrinking of the lattice, and removal results in expansion. Intriguingly, additional diffraction peaks appear

(Figure 2a,b, indicated by arrows) during the discharge process, around 80% depth of discharge (DoD), near 1.7 V (vs Zn, or  $\sim 0.93$  V vs SHE). These peaks can be indexed to (001), (002), and (003) peaks of the LDH-type  $Zn_4SO_4(OH)_6 \cdot 5H_2O$  phase that has been reported earlier as the byproduct of proton intercalation for several AZB cathodes.<sup>[10–13]</sup> The simultaneous formation of ZHS with  $H^+$  intercalation is what enables the tracking of  $H^+$  intercalation using *operando* XRD. The detection of

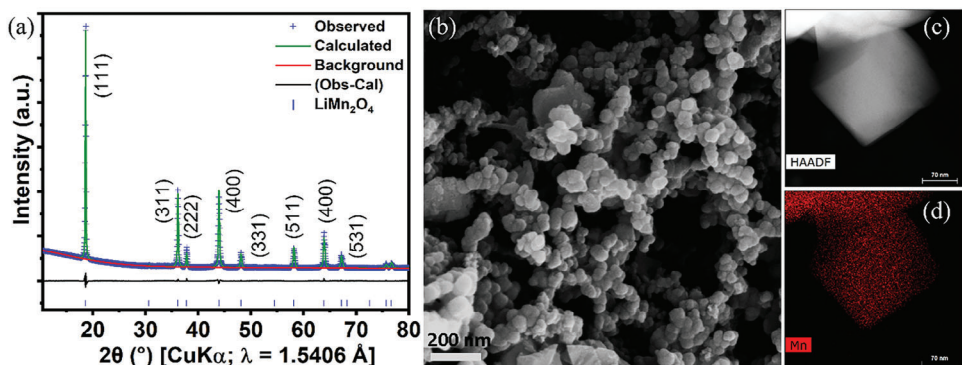


**Figure 1.** Structural and morphological characterization of the  $\text{LiMn}_2\text{O}_4$  material. (a) Rietveld refinement ( $R_{wp}$ : 3.3%) of the  $\text{LiMn}_2\text{O}_4$  structural model with laboratory powder XRD data of pristine commercially obtained  $\text{LiMn}_2\text{O}_4$  spinel. The observed data points (+ symbol); calculated profile (green line); difference profile (black line); Bragg positions (blue ticks). (b) A representative FE-SEM image of pristine  $\text{LiMn}_2\text{O}_4$ . (c) High angle annular dark field (HAADF) STEM image of a representative  $\text{LiMn}_2\text{O}_4$  particle and d) the corresponding EDX map showing Mn.

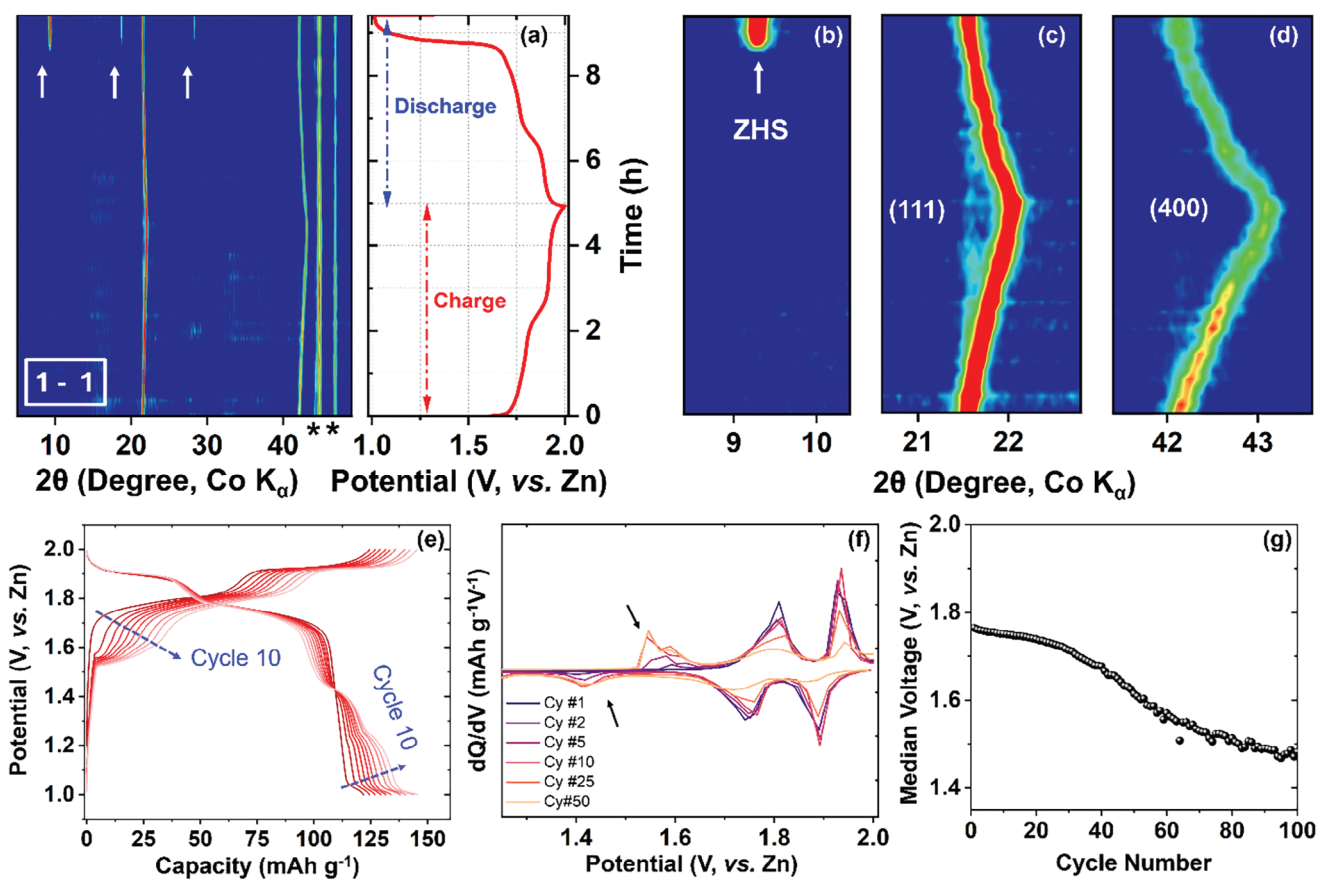


**Figure 2.**  $\text{LiMn}_2\text{O}_4$  charge storage mechanism and the consequence of  $\text{H}^+$ -mediated charge storage. (a) Operando XRD contour plot for  $\text{LiMn}_2\text{O}_4$  in a  $\text{LiMn}_2\text{O}_4||\text{Zn}$  cell with the 1-1 (M)  $\text{Li}_2\text{SO}_4\text{-ZnSO}_4$  electrolyte cycled at a 0.2 C rate and the corresponding galvanostatic charge-discharge profile. The asterisks on the  $2\theta$  axis label the diffraction peaks arising from the operando cell body. The evolution of the (b) ZHS peak and  $\text{LiMn}_2\text{O}_4$  (c) (111) and (d) (400) peaks upon charge-discharge. (e) The galvanostatic charge-discharge profile for the  $\text{LiMn}_2\text{O}_4||\text{Zn}$  cell with the 1-1 electrolyte, (f) the corresponding differential capacity profile during the first ten cycles, and (g) the median discharge voltage evolution as a function of cycling. The arrows in (f) point to the peaks arising at low voltages with increasing cycle numbers.

the ZHS phase suggests a significant extent of  $H^+$  intercalation in delithiated- $Li_xMn_2O_4$ , which occurs towards the end of the discharge below the median discharge potential ( $\sim 1.8$  V vs Zn). Interestingly,  $LiMn_2O_4$  was earlier believed to be an exclusively  $Li^+$  (de)intercalation system, and its charge storage mechanism was never critically probed. As the *operando* XRD experiment further reveals, even though the ZHS gets removed during the subsequent charge – through  $H^+$  deintercalation and ZHS dissolution – some remain at the end of the charge (Figure S2, Supporting Information).  $LiMn_2O_4$  structural evolution, on the other hand, appears to be fully reversible, as indicated by the return of the (111) and (400) peaks to their original  $2\theta$  positions.

$H^+$  co-intercalation mediated charge storage mechanism is common to oxide-type AZB cathodes, and the process is highly reversible to render long-term cyclability, particularly at high currents ( $> 1C$ ). Earlier, we predicted that reversibility and hence cyclability could become an issue under low current cycling,<sup>[12]</sup> which is rarely probed. Therefore, galvanostatic cycling of  $LiMn_2O_4$  was carefully probed at a moderate C/3 current rate in the 1-1 electrolyte, and the voltage profile for the first ten cycles is shown in Figure 2e. There is a clear evolution of the voltage profile, highlighted by the appearance of lower voltage steps during discharge and charge. These become further apparent in the differential capacity ( $dQ/dV$ ) profiles shown in Figure 2f. As the arrows in the figures indicate, the low-voltage redox steps/peaks intensify with cycling, leading to continuous degradation of the median (discharge) voltage (Figure 2g) – affecting a drop of  $\approx 0.3$  V over 100 cycles. This is equivalent to a nearly 17% decline in obtainable energy density if we assume the capacity to be constant. Here, the median discharge voltage is calculated by dividing the energy delivered during discharge by the discharge capacity. Notably, the discharge voltage decay occurs despite having a good Coulombic efficiency of  $\sim 99.5\%$  (discussed below).

## 2.2. Influence of $Li^+$ to $Zn^{2+}$ Ratio in the Electrolyte on the $LiMn_2O_4$ Charge Storage Mechanism

The electrolyte is expected to have a strong influence on the charge storage mechanism in aqueous batteries. While previous efforts on averting or suppressing  $H^+$  co-intercalation in AZB cathodes focused on reducing the  $H^+$  activity of the electrolyte by subduing its aqueous nature, given the dual-ionic system here, elucidating the impact of varying  $Li^+$  ( $Li_2SO_4$ ) to  $Zn^{2+}$  ( $ZnSO_4$ ) ratio in the electrolyte on the charge storage mechanism is necessary. In this regard, 0.1 M  $Li_2SO_4$  – 1.9 M  $ZnSO_4$  (0.1-1.9) and 1.75 M  $Li_2SO_4$  – 0.25 M  $ZnSO_4$  (1.75–0.25) were chosen as  $Zn^{2+}$ -rich and  $Li^+$ -rich electrolytes, respectively and 1.25–0.75 and 1.5–0.5 served as electrolytes with moderately high  $Li^+$  to  $Zn^{2+}$  ratio (compared to the reference 1-1 electrolyte). The 0.875–0.125 electrolyte composition, which has the same  $Li^+$  to  $Zn^{2+}$  ratio as the 1.75–0.25 electrolyte, was also investigated to probe the influence of the  $Li^+$  concentration in the electrolyte. Since the 1-1 electrolyte already leads to  $H^+$  intercalation, other electrolytes with lower  $Li_2SO_4$  to  $ZnSO_4$  concentration ratios will lead to the same mechanism and were not studied.

Figure 3a–d shows the *operando* XRD evolution of the  $LiMn_2O_4$  cathode in the 0.1-1.9 electrolyte. As with the 1-1 electrolyte, the ZHS diffraction peaks appear at around  $\sim 1.7$  V, but the peaks be-

gin to form early ( $\sim 65\%$  DOD) into the discharge here compared to that in the 1-1, leading to a greater extent of  $H^+$  intercalation in the 0.1-1.9 compared to that in the 1-1. Regardless, the evolution of  $LiMn_2O_4$  as a function of charge/discharge stays identical with the same shift in the lattice parameter ( $\Delta a$ :  $\sim 0.17$  –  $0.18$  Å) during charge/discharge, which suggests that  $Li^+$  and  $H^+$  intercalation has the same effect on the spinel structure. Not surprisingly, in the absence of  $Li^+$  in the electrolyte (with the 0–2 electrolyte), ZHS formation starts very early during the discharge, preceded by a very brief  $Li^+$  intercalation segment with a large hysteresis, indicating a dominant  $H^+$ -intercalation mediated charge storage (Figure S3, Supporting Information). While initially there is no  $Li^+$  in the electrolyte,  $Li^+$  de-intercalated during charge intercalates back during discharge, but the small  $Li^+$  concentration leads to the observed high overpotential. Interestingly, a mechanistic change is observed upon increasing the  $Li^+$  to  $Zn^{2+}$  ratio. As evident from Figure 3e–g, with the 1.75–0.25 electrolyte, the ZHS peaks are not observed at all in the *operando* XRD data, suggesting an overhaul of the charge storage mechanism. In fact, ZHS signals are also absent for the 1.5–0.5 (Figure S4, Supporting Information) and the 1.25–0.75 (Figure 3h–j) electrolytes, which indicates that a  $Li_2SO_4$  to  $ZnSO_4$  molar ratio higher than 1:1 is enough to suppress a considerable  $H^+$  intercalation, revealed as ZHS XRD signals. The fact that the ZHS diffraction peaks do not also appear on the *operando* plot for the 0.875–0.125 electrolyte (Figure S5, Supporting Information; same  $Li^+$ /Zn $^{2+}$  ratio as the 1.75–0.25 electrolyte) confirms that it is the  $Li^+$  to  $Zn^{2+}$  ratio and not the absolute  $Li^+$  concentration which dictates the charge storage mechanism, at least when the overall salt concentration is  $\approx 1$  M. The  $LiMn_2O_4$  lattice parameter as a function of charge/discharge, as tracked from the Rietveld analysis of the *operando* XRD datasets for 0.1–1.9, 1-1, and 1.75–0.25 electrolytes (Figure S6, Supporting Information), further illustrate that the magnitude of structural change ( $\Delta a$ ) is very similar irrespective of the type of the intercalant ion even though the potential is, on average, highest for 1.75–0.25 followed by 1-1 and then 0.1–1.9. This observation indicates that it is likely not the size of the two monovalent cations but the intercalant cation-mediated modulation of the Coulomb interaction in the oxide lattice that dictates the structural evolution.

Even though *operando* XRD does not reveal the formation of the ZHS phase for the  $Li_2SO_4$ - $ZnSO_4$  electrolytes with greater than 1-1 concentration, it could still form at levels not sufficient enough to show up on the XRD pattern. Considering that the ZHS byproduct is known to have a distinct flake-like morphology, we investigated discharged  $LiMn_2O_4$  cathode ex situ by SEM. Not surprisingly, the 0.1–1.9 electrolyte results in the accumulation of a large amount of thin ZHS flakes on the surface of the cathode, which are also identified from strong Zn and S signal under EDX elemental mapping, presented alongside the SEM image (Figure 4a). As revealed in Figure 4b, a significant ZHS coverage is also observed for the 1-1 electrolyte, which is consistent with the *operando* XRD observation. Interestingly, ZHS flakes are noticeable even for the 1.25–0.75 electrolyte (Figure 4c), which the *operando* XRD fails to capture. Importantly, the 1.75–0.25 electrolyte renders a nearly ZHS-free discharged electrode, although a few small flakes can still be found (Figure 4d), consistent with the quantitative analysis presented below. It must be noted that some areas of the electrode surface were free of ZHS flakes under

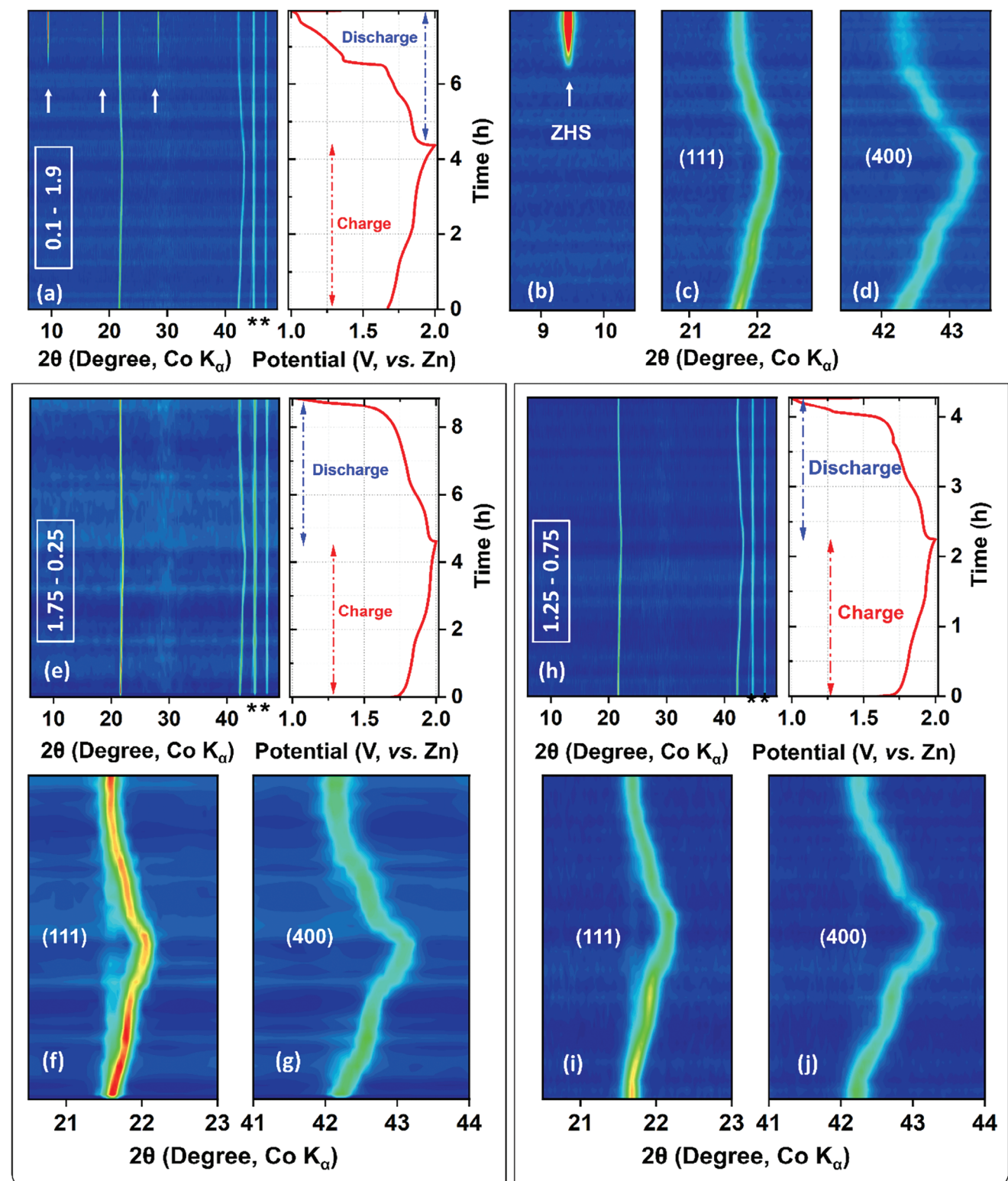


**Figure 3.** Regulating H<sup>+</sup>-mediated charge storage in LiMn<sub>2</sub>O<sub>4</sub> by tuning Li<sup>+</sup> to Zn<sup>2+</sup> concentration ratio in the electrolyte. *In operando* XRD contour plot for LiMn<sub>2</sub>O<sub>4</sub> in a LiMn<sub>2</sub>O<sub>4</sub>||Zn cell with (a–d) 0.1–1.9, (e–g) 1.75–0.25, and (h–j) 1.25–0.75 electrolytes, cycled at a 0.2 C rate and the corresponding galvanostatic charge-discharge profile. The H<sup>+</sup> intercalation byproduct ZHS diffraction peaks are labeled with the arrows. The asterisks on the 2θ axis point to the diffraction peaks from the *operando* cell body. The evolution of the (b) ZHS peak, (c,f,i) the LiMn<sub>2</sub>O<sub>4</sub> (111) peak, and (d,g,j) LiMn<sub>2</sub>O<sub>4</sub> (400) peak upon charge-discharge.

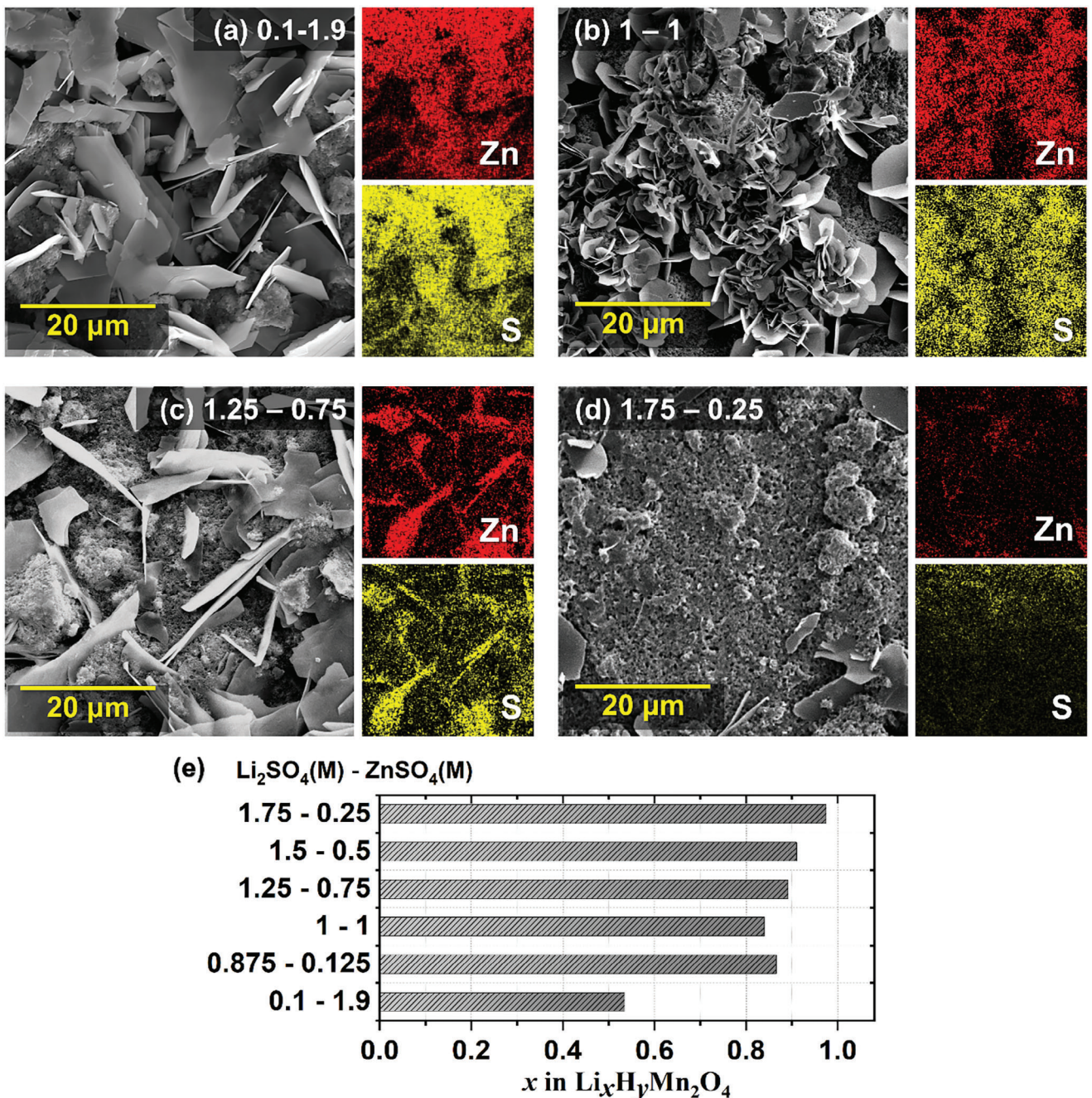


**Figure 4.** Postmortem analysis of cycled  $\text{LiMn}_2\text{O}_4$  electrodes. Representative SEM images and EDX elemental mapping for  $\text{LiMn}_2\text{O}_4$  electrode after discharge in (a) 0.1-1.9, (b) 1-1, (c) 1.25-0.75, and (d) 1.75-0.25  $\text{Li}_2\text{SO}_4$ - $\text{ZnSO}_4$  electrolytes. The flaky material observed under SEM is  $\text{Zn}_4\text{SO}_4(\text{OH})_6 \cdot \text{nH}_2\text{O}$  formed as a result of  $\text{H}^+$  intercalation. As expected, the flakes have strong zinc and sulfur signals. (e) Li-composition of the cycled  $\text{LiMn}_2\text{O}_4$  electrodes after discharge as revealed by ICP-OES analysis.

SEM, but we show the flakes to be wholly transparent about our observation. Given that the ZHS flakes appear almost exclusively on the electrode surface, even a very small percentage of  $\text{H}^+$  intercalation will lead to a few visible flakes, as we observe here for the 1.75-0.25 electrolyte. Upon charging in the 1.75-0.25 electrolyte, the  $\text{LiMn}_2\text{O}_4$  electrode reverts back to the pristine state, which is not the case for the 1-1 electrolyte, where a considerable amount of the ZHS byproduct remains visible after charging (Figure S7,

Supporting Information). This observation agrees with *operando* XRD results, which revealed incomplete dissolution (removal) of the ZHS upon charging in the 1-1 electrolyte.

While SEM provides a direct visual confirmation of the byproduct formation, for a quantitative estimation of the extent of  $\text{Li}^+$  (and  $\text{H}^+$ ) storage, the electrodes were assessed by inductively coupled plasma optical emission spectroscopy (ICP-OES) analysis. Evaluation of Li to Mn ratio in the discharged cathode confirmed

the extent of  $\text{Li}^+$  storage upon discharge. As evident from Figure 4e and Table S1 (Supporting Information), which presents the  $\text{Li}^+$  stoichiometry in the discharged  $\text{LiMn}_2\text{O}_4$  after the second discharge, the 1.75–0.25 electrolyte results in almost exclusive (98%)  $\text{Li}^+$  intercalation compared to 84%  $\text{Li}^+$  (or 16%  $\text{H}^+$ ) intercalation in the 1-1 electrolyte. As expected, 1.25–0.75 and 1.5–0.5 electrolytes also result in greater  $\text{Li}^+$  (so, lower extent of  $\text{H}^+$ ) intercalation compared to the 1-1 electrolyte. The 0.875–0.125 electrolyte with half the  $\text{Li}^+$  and  $\text{Zn}^{2+}$  concentration of 1.75–0.25 but the same  $\text{Li}^+/\text{Zn}^{2+}$  concentration ratio also enhances  $\text{Li}^+$  storage but not to the same extent as 1.75–0.25, which alludes to the necessity of a relatively high Li-salt concentration to suppress  $\text{H}^+$  intercalation comprehensively. Lithium composition of the  $\text{Li}_x\text{Mn}_2\text{O}_4$  cathode in 1-1 vis-à-vis 1.75–0.25 electrolyte was also investigated by ICP-OES as a function of the discharge voltage (Table S2, Supporting Information) to obtain insight into the competitive  $\text{Li}^+/\text{H}^+$  intercalation around and below 1.7 V, when the ZHS byproduct appears on the *operando* XRD. Until 1.85 V (vs Zn), the Li composition in the cathode remains comparable between the two electrolytes ( $x \approx 0.54$ –0.57 in  $\text{Li}_x\text{Mn}_2\text{O}_4$ ), indicating exclusive  $\text{Li}^+$  intercalation until 1.85 V. However, the lithium stoichiometry is noticeably different by 1.75 V, namely,  $x \approx 0.86$  and 0.72 in  $\text{Li}_x\text{Mn}_2\text{O}_4$  with 1.75–0.25 and 1-1 electrolytes, respectively. Considering that the 1.75–0.25 electrolyte leads to a greater extent of  $\text{Li}^+$  intercalation, it can be concluded that the 1-1 electrolyte renders a nearly equal extent of  $\text{Li}^+$  and  $\text{H}^+$  intercalation in the 1.85–1.75 V window. However, this  $\text{H}^+$  intercalation does not appear in *operando* XRD as the corresponding ZHS byproduct, as its amount on the cathode surface is still relatively low for detection. Below 1.5 V, the Li stoichiometry remains unchanged in the 1-1 electrolyte even though nearly 10% of the discharge capacity appears in the 1.5–1 V window (Figure 3e), indicating exclusive  $\text{H}^+$  intercalation below 1.5 V in the 1-1 electrolyte.

The pH of the electrolytes (Table S3, Supporting Information) was also probed to check for possible influence on the  $\text{H}^+$  intercalation. While all electrolytes are mildly acidic (pH: 4.4–5.7), increasing  $\text{Li}_2\text{SO}_4$  concentration increases the pH of the electrolyte. However, considering the very low  $\text{H}^+$  concentration ( $10^{-4}$ – $10^{-5}$  M) relative to that of  $\text{Li}^+$  ( $> 1$  M), the bulk  $\text{H}^+$  concentration in the electrolyte (or pH) is likely to have little to no effect on the charge storage behavior. Besides, the fact that 1.75–0.25 electrolyte is more effective compared to 0.875–0.125 in suppressing  $\text{H}^+$  intercalation despite the latter having a higher pH further attests to the minor influence of the electrolyte pH.

### 2.3. Averting $\text{H}^+$ -Mediated Charge Storage Stabilizes the High Output Voltage of $\text{LiMn}_2\text{O}_4$

Based on the combination of the *operando* XRD and ex situ analytical techniques, it is evident that the 1.75–0.25 electrolyte results in almost complete suppression of  $\text{H}^+$  co-intercalation. But to test whether that can avert the voltage decay and improve the cyclability, galvanostatic charge-discharge cycling was performed. The cells were cycled at a C/3 rate with both small ( $\approx 3$  mg cm $^{-2}$ ) and high ( $10$  mg cm $^{-2}$ ) active cathode mass loading, and the results for the 1.75–0.25 electrolyte were compared against the 1-1 electrolyte. In contrast to the 1-1 electrolyte (Figure 2e), the voltage response remains steady with the 1.75–0.25 electrolyte, as

shown for the first 10 cycles in Figure 5a, with no lower voltage (< 1.7 V) plateau evolution as observed with the 1-1 electrolyte. The same is evident from the corresponding differential capacity or dQ/dV plot in Figure 5b. A slight evolution is observed for the lower voltage reduction peak (cathodic peak), but the peak shift is upward, which leads to a small increase in the discharge voltage during the initial cycles. In fact, all peaks show a little blue (upward) shift, which most likely stems from a subtle structural rearrangement. Thanks to the steady voltage response, the median discharge voltage shows negligible degradation over long-term cycling (Figure 5c) with the 1.75–0.25 electrolyte. In agreement with the observation from the dQ/dV data, a slight increase in the median discharge voltage is noticed here. The cyclability also improves with the 1.75–0.25 electrolyte, as evident from  $\approx 79\%$  capacity retention with a stable Coulombic efficiency (CE) of  $\approx 99.8\%$  compared to only 50% retention and fluctuating CE in the 1-1 electrolyte (Figure 5d) at a low ( $\approx 3$  mg cm $^{-2}$ ) cathode loading. A similarly steady voltage response is observed with the 1.75–0.25 electrolyte at high ( $\approx 10$  mg cm $^{-2}$ )  $\text{LiMn}_2\text{O}_4$  loading, leading to a stable discharge voltage and improved capacity retention with cycling compared to the 1-1 electrolyte under the same conditions.

Interestingly, at a high cathode loading, the median voltage decay for the 1-1 electrolyte is considerably less compared to that at a low loading, which stems from the relatively high areal current density – 0.5 mA cm $^{-2}$  compared to 0.15 mA cm $^{-2}$  at a low loading – that slows down the somewhat sluggish  $\text{H}^+$  intercalation as revealed by impedance analysis as a function of state of charge (Figure S8, Supporting Information). This result also explains why probing the cycling at a higher C rate (1C is already 0.45 mA cm $^{-2}$  current for a small 3 mg cm $^{-2}$   $\text{LiMn}_2\text{O}_4$  loading) can lead to improved behavior, as often presented in previous literature. Considering that stable performance at low currents is as essential as at high currents, the discharge voltage (and hence the available energy density) and cycling stability showcased here with the modified 1.75–0.25 electrolyte owing to the complete suppression of  $\text{H}^+$  co-intercalation is striking. The fact that the  $\text{H}^+$  intercalation can be suppressed without altering the electrolyte's aqueous nature, as demonstrated here for the first time, is fundamentally and practically exciting. As expected, other electrolytes with higher than 1:1  $\text{Li}_2\text{SO}_4$  to  $\text{ZnSO}_4$  ratio can also stabilize the median voltage (Figure S9, Supporting Information), but not to the same extent as 1.75–0.25, simply because  $\text{H}^+$  co-intercalation is not entirely suppressed, and that leads to slight degradation of the voltage profile with cycling (Figure S10, Supporting Information).

### 2.4. Rationalizing $\text{LiMn}_2\text{O}_4$ 's $\text{H}^+$ Co-Intercalation Chemistry and Its Suppression

In order to cross-validate the observations of  $\text{Li}^+$ - $\text{H}^+$  co-intercalation, particularly at a low  $\text{Li}^+$  to  $\text{Zn}^{2+}$  ratio in the electrolyte (i.e., 1-1, 0.1–1.9, and 0–2), DFT calculations were performed at different Li, H, and Zn concentrations within the spinel- $\text{Mn}_2\text{O}_4$  framework. Specifically, the compositions of  $x = 0$ , 0.25, 0.5, 0.75, and 1 were considered for  $\text{A}_x\text{Mn}_2\text{O}_4$  ( $\text{A} = \text{Li}, \text{H}$ , or  $\text{Zn}$ ). The DFT-calculated pseudo-binary convex hulls at 0 K are displayed in Figure S11 (Supporting Information), and the

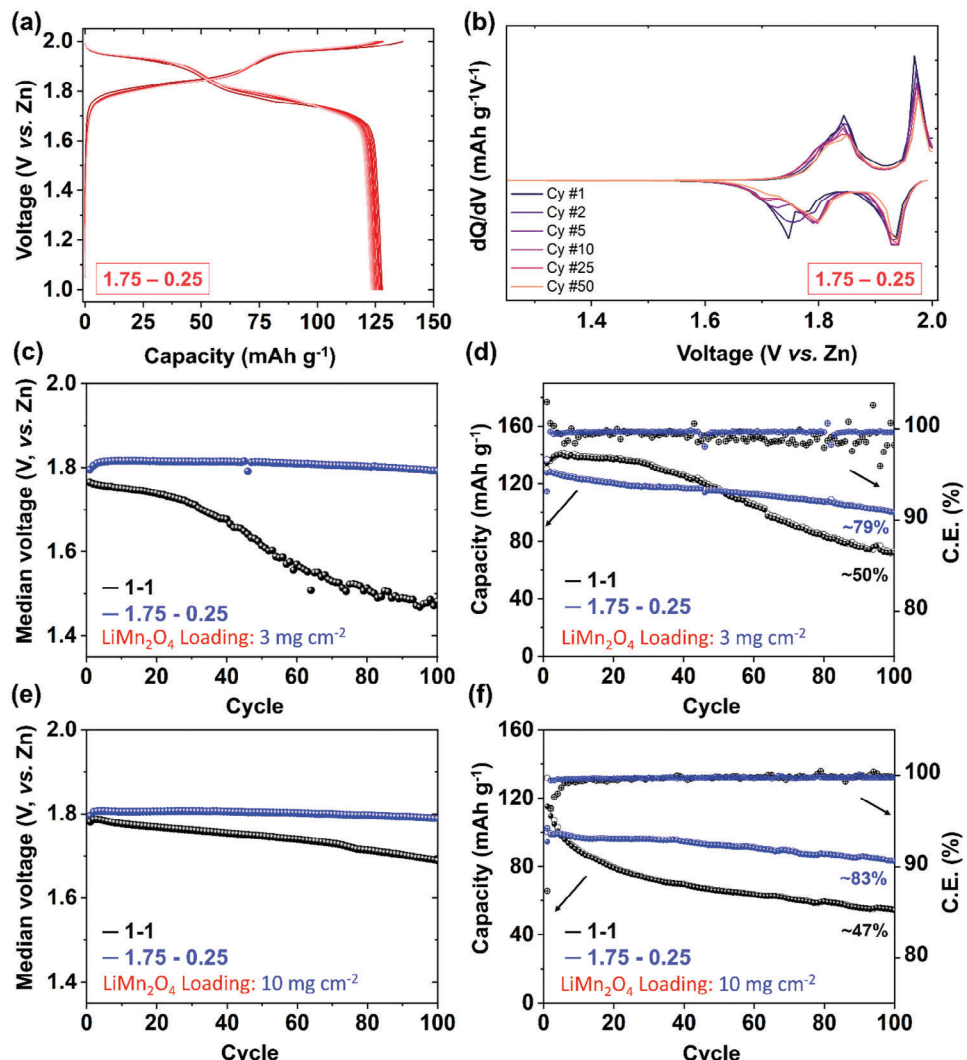


**Figure 5.** Prevention of H<sup>+</sup>-mediated charge storage leads to a stable voltage output and improved cycling stability. a) The galvanostatic charge-discharge profile for the LiMn<sub>2</sub>O<sub>4</sub>||Zn cell with the 1.75–0.25 (M) Li<sub>2</sub>SO<sub>4</sub>–ZnSO<sub>4</sub> electrolyte and b) the corresponding differential capacity profile during the first ten cycles. c,e) The median discharge voltage evolution as a function of cycling for 1-1 vis-à-vis 1.75–0.25 electrolyte and (d,f) the corresponding capacity retention and Coulombic efficiency. Data in (c, d) and (e, f) are at a low (~3 mg cm<sup>-2</sup>) and a high (~10 mg cm<sup>-2</sup>) active LiMn<sub>2</sub>O<sub>4</sub> loading at the cathode, respectively.

corresponding intercalation voltage profiles are plotted in Figure 6. The pseudo-binary convex hulls are referenced to the Mn<sub>2</sub>O<sub>4</sub> and AMn<sub>2</sub>O<sub>4</sub> compositions, while the voltages are plotted with respect to the Zn electrode (−0.76 V vs SHE). Note that DFT calculations are known to overestimate experimental intercalation voltages, but the qualitative trends observed in the calculations should be consistent with experiments.<sup>[31,32]</sup>

It is apparent that Zn<sup>2+</sup> intercalation in Mn<sub>2</sub>O<sub>4</sub> is expected to occur via a two-phase mechanism, with cubic-Mn<sub>2</sub>O<sub>4</sub> and tetragonal-ZnMn<sub>2</sub>O<sub>4</sub> being the ground state configurations (Figure S11c, Supporting Information), at an average voltage of 1.62 V versus Zn (0.85 V vs SHE, Figure 6c). Thus, Zn<sup>2+</sup> intercalation in Mn<sub>2</sub>O<sub>4</sub> exhibits a lower thermodynamic driving force compared to Li<sup>+</sup> intercalation (average voltage of 2.32 V vs Zn, Figure 6a), or H<sup>+</sup> intercalation (2.13 V vs Zn, Figure 6b). Moreover, Zn<sup>2+</sup> is expected to diffuse poorly in oxide spinel lattices, given the preferential tetrahedral coordination environment of Zn.<sup>[32]</sup> Whereas, monovalent ions, such as Li<sup>+</sup> and H<sup>+</sup>, are nominally expected to exhibit swifter diffusion within oxide spinels.<sup>[4,32]</sup> Additionally, a two-phase intercalation mechanism requires the creation and propagation of a phase boundary, between the cubic-Mn<sub>2</sub>O<sub>4</sub> and tetragonal-ZnMn<sub>2</sub>O<sub>4</sub> domains in the Zn<sub>x</sub>Mn<sub>2</sub>O<sub>4</sub> system, which also slows the kinetics of the reaction and/or increases the overpotential during intercalation, similar to observations in the Li<sub>x</sub>FePO<sub>4</sub> system.<sup>[33,34]</sup> Thus, we expect Zn<sup>2+</sup> to not only be thermodynamically unfavored but also kinetically sluggish in comparison to Li<sup>+</sup> and H<sup>+</sup>, for intercalation into Mn<sub>2</sub>O<sub>4</sub>. Thus, any contributions of Zn<sup>2+</sup> (de)intercalation to the observed electrochemical data within the experiments should be negligible. Also, sole Zn<sup>2+</sup> intercalation is expected to occur only in systems that have negligible H<sup>+</sup> (nonaqueous) and Li<sup>+</sup> in the electrolyte.

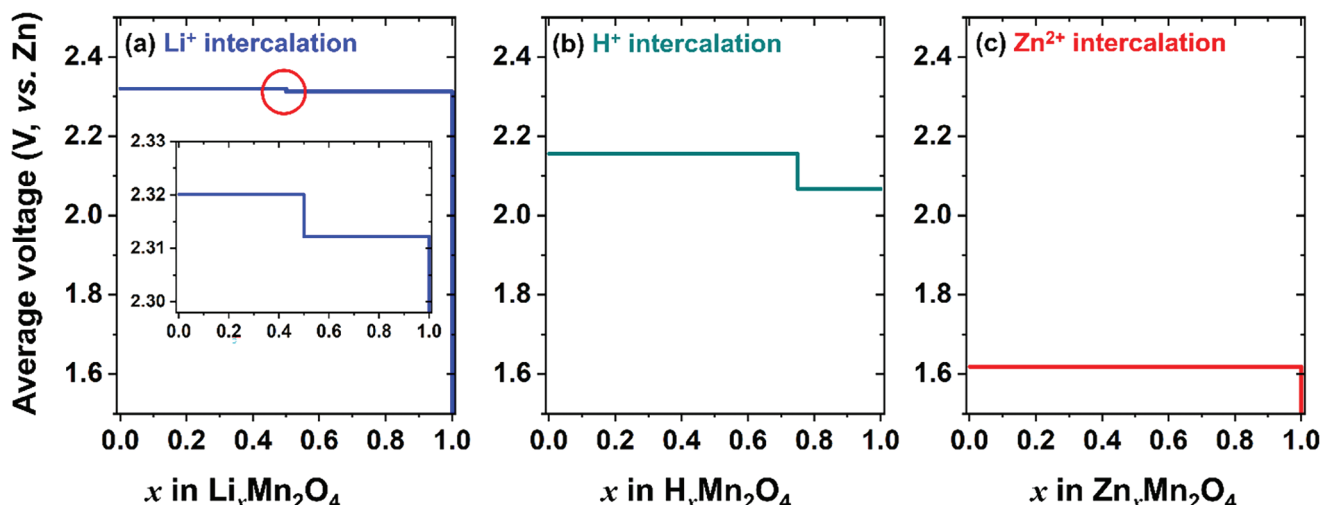


**Figure 6.** DFT analysis of  $\text{Li}^+$ ,  $\text{H}^+$ , and  $\text{Zn}^{2+}$  intercalation into  $\text{Mn}_2\text{O}_4$  spinel. The average voltage curves at 0 K for (a)  $\text{Li}_x\text{Mn}_2\text{O}_4$  phases, (b)  $\text{H}_x\text{Mn}_2\text{O}_4$  phases, and (c)  $\text{Zn}_x\text{Mn}_2\text{O}_4$  phases obtained from the respective hulls as a function of  $\text{Li}^+/\text{H}^+/\text{Zn}^{2+}$  concentration. The voltage curves are plotted against  $\text{Zn}/\text{Zn}^{2+}$  potential, and the intercalating ion concentration in the system is denoted by  $x$ .

In the case of  $\text{Li}^+$  and  $\text{H}^+$  intercalation into  $\text{Mn}_2\text{O}_4$ , both cations are expected to have similar driving forces for intercalation, with  $\text{Li}^+$  being slightly more favored compared to  $\text{H}^+$ , as indicated by the calculated average voltages. Thus, given the presence of both  $\text{Li}^+$  and  $\text{H}^+$  in the electrolyte, we expect  $\text{Li}^+$  intercalation to occur first, followed by either  $\text{H}^+$  intercalation or  $\text{Li}^+$  and  $\text{H}^+$  co-intercalation, in agreement with our experimental observations. Also, both  $\text{Li}^+$  and  $\text{H}^+$  intercalation exhibit ground states at intermediate concentrations, namely,  $\text{Li}_{0.5}\text{Mn}_2\text{O}_4$  (Figure S11a, Supporting Information) and  $\text{H}_{0.75}\text{Mn}_2\text{O}_4$  (Figure S11b, Supporting Information), apart from the  $\text{Mn}_2\text{O}_4$  and  $\text{AMn}_2\text{O}_4$  ( $\text{A} = \text{Li}$  or  $\text{H}$ ) compositions, which indicates a different phase behavior compared to  $\text{Zn}_x\text{Mn}_2\text{O}_4$ . Moreover, both  $\text{Li}_x\text{Mn}_2\text{O}_4$  and  $\text{H}_x\text{Mn}_2\text{O}_4$  exhibit several configurations that are  $< 50$  meV/atom above the computed convex hull, indicating the possibility of a solid-solution behavior during (de)intercalation at higher temperatures,<sup>[35]</sup> in qualitative agreement with our experimental trends.

With respect to kinetics, although  $\text{Li}^+$  and  $\text{H}^+$  should exhibit facile bulk diffusivity within the  $\text{Mn}_2\text{O}_4$  cathode, we expect  $\text{H}^+$  intercalation to be slowed down due to the formation of the ZHS byproduct, which is not the case for  $\text{Li}^+$  intercalation. This is experimentally observed from the diffusion coefficient values determined by the galvanostatic intermittent titration technique or GITT (Figure S12, Supporting Information). In the case of the 1-1 electrolyte, the ion diffusion coefficient falls an order of magnitude below that for the 1.75–0.25 electrolyte during the last and fast 20% of the discharge and charge, respectively, indicating that the  $\text{H}^+$  (de)intercalation kinetics is considerably sluggish compared to the  $\text{Li}^+$  (de)intercalation in  $\text{LiMn}_2\text{O}_4$ . The same is also apparent from the GITT voltage profile, which shows larger voltage spikes (jump in steady-state voltage) in the  $\text{H}^+$  (de)intercalation region for the 1-1 electrolyte. In contrast, 1.75–0.25 displays a uniform voltage response across the GITT profile. It is important to note that the employed electrolytes are only mildly acidic (Table S3, Supporting Information), which results in four to five orders of magnitude difference in the concentra-

tion (and hence availability) of  $\text{H}^+$  compared to  $\text{Li}^+$  in the electrolyte. Thus, for a sizeable quantity of  $\text{H}^+$  intercalation to occur within  $\text{Mn}_2\text{O}_4$ , the formation of the ZHS byproduct is necessary since ZHS traps  $\text{OH}^-$  left behind after  $\text{H}^+$  intercalation and does not let the electrolyte become alkaline.<sup>[12]</sup> If the formation or dissolution of ZHS is slowed kinetically, which can occur when the electrode is cycled at high rates,  $\text{H}^+$  intercalation or deintercalation will also be slowed, which also explains the suppressed  $\text{H}^+$  intercalation in  $\text{Li}_x\text{Mn}_2\text{O}_4$  under high rates (see above). Note that ZHS formation also depends on the availability of  $\text{Zn}^{2+}$  in the electrolyte. Thus, any reduction in  $\text{Zn}^{2+}$  concentration in the electrolyte should impede the formation of ZHS on the electrode surface, thus mitigating  $\text{H}^+$  intercalation, supporting the experimental observations of negligible  $\text{H}^+$  intercalation in a Li-rich (1.75–0.25) electrolyte. Thus, disfavoring the formation/dissolution of ZHS, either by cathode surface modifications and/or reducing the availability of  $\text{Zn}^{2+}$ , is an effective strategy to suppress  $\text{H}^+$  intercalation. A direct consequence of this differential kinetics becomes apparent in the rate capability data for the two electrolytes (Figure S13, Supporting Information). While the cell with 1-1 electrolyte shows higher capacity than with 1.75–0.25 electrolyte at lower current rates, the trend reverses at higher current rates.

## 2.5. The Origin of $\text{H}^+$ Intercalation-Mediated Voltage Decay and Its Prevention

First, differential manganese dissolution-mediated performance variation between 1-1 and 1.75–0.25 was ruled out by performing the ICP-OES analysis of the cycled electrolyte (Figure S14, Supporting Information). Both electrolytes led to comparable and very small manganese dissolution. Therefore, the  $\text{LiMn}_2\text{O}_4$  phase evolution upon cycling in the two electrolytes was probed by synchrotron X-ray diffraction of the discharged electrodes after 5, 50, and 100 cycles. The difference between the  $\text{LiMn}_2\text{O}_4$  electrodes cycled in the two electrolytes is apparent even after

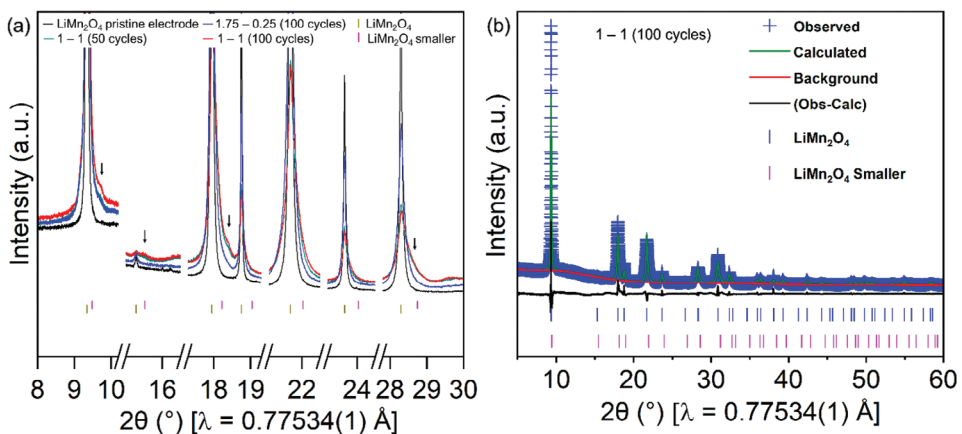


**Figure 7.** Synchrotron XRD investigation of the cycled  $\text{LiMn}_2\text{O}_4$  electrode. (a) Synchrotron XRD pattern for the pristine electrode (black), electrodes cycled in the 1-1 electrolyte for 50 cycles (green) and 100 cycles (red), and the electrode cycled in the 1.75–0.25 electrolyte for 100 cycles (blue) overlaid on top of each other. The vertical lines – magenta and yellow-green – represent the spinel  $\text{LiMn}_2\text{O}_4$  phase and  $\text{LiMn}_2\text{O}_4$  phase with a smaller lattice parameter, respectively. The spinel phase with the smaller lattice parameter is used to fit the shoulders (marked by arrows) on the parent spinel  $\text{LiMn}_2\text{O}_4$  peaks. (b) Rietveld refinement using structural models and synchrotron powder XRD data of the electrode cycled in the 1-1 electrolyte for 100 cycles. The symbols used in the plot are denoted inside the figure.

5 cycles (Figure S15, Supporting Information). For the 1-1 electrolyte with  $\text{H}^+$  co-intercalation, shoulders on the  $\text{LiMn}_2\text{O}_4$  peaks appear, and the peak intensity reduces compared to that with the 1.75–0.25 electrolyte, where  $\text{H}^+$  intercalation is averted. This provides some evidence of an irreversible phase transition in 1-1 with  $\text{H}^+$ -mediated charge storage. The phase evolution in the 1-1 electrolyte becomes further evident after 50 and 100 cycles, as shown in Figure 7a, with heightened shoulder intensity and diminished intensity for the  $\text{LiMn}_2\text{O}_4$  peaks. Interestingly, for the electrode cycled in the 1.75–0.25 electrolyte, shoulders become visible after 100 cycles, albeit the intensity is much lower than that for the 1-1 electrolyte, indicating parasitic  $\text{H}^+$  storage kicking in after longer-term cycling. This is not entirely unexpected, given the slow cycling rate (C/3) and the aqueous electrolyte.

Further, we performed Rietveld analysis using the  $\text{LiMn}_2\text{O}_4$  structural model and the synchrotron XRD data. In the case of the 1-1 electrolyte, for both 50 and 100-cycle data, two  $\text{LiMn}_2\text{O}_4$  (spinel) models could be used in the refinement, with the second component being minor in phase fraction and having a smaller lattice parameter (Figure 7b; Figure S16, Supporting Information). Notably, the phase fraction for the second spinel phase grows from 50 cycles (~2.7%) to 100 cycles (~9%), suggesting significant phase growth, which can be attributed to the extent of active  $\text{LiMn}_2\text{O}_4$  degradation with cycling (Table S4, Supporting Information). In comparison, refinement of the 100-cycle data from the 1.75–0.25 electrolyte suggests only ~1% secondary phase, consistent with the highly suppressed  $\text{H}^+$ -mediated charge storage. Since the shoulders are somewhat broad (Figure 7a), the peaks may correspond to more than one secondary phase or a smaller particle size for this/these phases. This impacts the precise determination of the lattice parameters of the secondary phase that irreversibly forms with cycling as a result of the  $\text{H}^+$  co-intercalation. In the case of the 1-1 electrolyte, in addition to the shoulders, additional peaks are observed in the cycled patterns, which can be modeled with  $\text{Mn}_3\text{O}_4$ . The presence of this phase can explain the increasing low-voltage (<1.5 V) redox activity leading to declining average discharge voltage. It is likely that

the  $\text{H}^+$  intercalated spinel  $\text{Mn}_2\text{O}_4$ , that is,  $\text{HMn}_2\text{O}_4$ , decomposes to  $\text{Mn}_3\text{O}_4$  that displays a voltage response in AZBs,<sup>[36]</sup> which is consistent with the lower voltage discharge and charge steps observed for  $\text{LiMn}_2\text{O}_4$  cycling when  $\text{H}^+$ -mediated charge storage is significant.

### 3. Conclusion

The hitherto unknown  $\text{H}^+$ -intercalation chemistry into spinel  $\text{LiMn}_2\text{O}_4$  cathodes in AZBs is disclosed here, and the influence of  $\text{Li}^+$  to  $\text{Zn}^{2+}$  concentration in the electrolyte is revealed by *operando* XRD, SEM, and quantitative ICP-OES analysis. While thermodynamic driving forces favor both  $\text{Li}^+$  and  $\text{H}^+$  intercalation into delighted spinel  $\text{Li}_x\text{Mn}_2\text{O}_4$ ,  $\text{H}^+$ -intercalation is found to proceed at a slightly lower potential compared to that of  $\text{Li}^+$  by DFT calculations. The theoretical prediction is consistent with the experimental data, showing  $\text{H}^+$  co-intercalation to be particularly dominant below 1.7 V (against Zn), which leads to the appearance of new lower voltage cathodic and anodic peaks with cycling and results in the median discharge voltage decay. This voltage decay is more severe at lower currents, a critical barrier for practical applications. Higher than 1-1  $\text{Li}^+$  to  $\text{Zn}^{2+}$  ratio electrolytes are shown to suppress  $\text{H}^+$ -electrochemistry due to the ability to slow down  $\text{H}^+$ -kinetics, directly linked to the kinetics of ZHS formation/dissolution. The 1.75–0.25  $\text{Li}^+$ - $\text{Zn}^{2+}$  electrolyte almost exclusively shuts down the  $\text{H}^+$ -intercalation, as revealed by ~98%  $\text{Li}^+$  in the cycled  $\text{LiMn}_2\text{O}_4$ , and stabilizes the median discharge voltage (1.8 V) as a function of cycling and improves the cycling stability at both low and high cathode loading. As revealed by synchrotron XRD-based postmortem analysis, the  $\text{H}^+$ -mediated charge storage leads to the irreversible transformation of  $\text{LiMn}_2\text{O}_4$  to a secondary spinel phase with a slightly smaller lattice parameter and lower voltage platform than the parent  $\text{LiMn}_2\text{O}_4$ , which is hindered by averting of  $\text{H}^+$ -mediated charge storage. Manipulating the  $\text{Li}^+/\text{Zn}^{2+}$  ratio in the electrolyte presents a unique and practical approach to preventing the damaging

$H^+$  electrochemistry and stabilizing the high voltage and high energy  $LiMn_2O_4$  cathode for aqueous battery application.

## 4. Experimental Section

The active cathode material  $LiMn_2O_4$  (MTI Corp, CA, USA) was mixed with carbon (Super P Carbon, TIMCAL) in 75:20 mass ratio in a mixer mill (Retsch MM 400). The ground mixture was mixed with polyvinylidene difluoride (PVDF) binder (sourced from Merck Millipore) in a 95:5 mass ratio using a small amount of N-Methyl-2-pyrrolidone (NMP) to obtain a thick and smooth slurry which was cast on graphite foil (0.254 mm thickness; Alfa Aesar, 99.8%) and dried in a vacuum oven for 12 h at 85 °C. 1 cm<sup>2</sup> coins were punched out and used as the positive electrode (cathode). The average active material loading was  $\approx 3 \text{ mg cm}^{-2}$ . 10 mg cm<sup>-2</sup> active loading coins were used for high-loading cells. For *operando* XRD, the as-prepared slurries were cast onto a glassy carbon disk (0.785 cm<sup>2</sup> area, 50 μm thickness) and dried under vacuum for 12 h at 85 °C.

Galvanostatic cycling was performed in two-electrode Swagelok®-type cells with titanium rod current collectors on a VMP3 (Biologic) potentiostat/galvanostat and LAND CT2001A battery cyclers in 1–2 V (against Zn) potential window. For *operando* XRD investigation, a home-built titanium body cell with a glassy carbon window was used, and the galvanostatic cycling was performed with a portable PalmSens4 potentiostat/galvanostat. All electrochemical cycling was performed at room temperature (22 ± 1 °C) against a metallic zinc coin anode (20/100 μm thickness) employing a glass fiber type separator (Merck Millipore; thickness: 190 μm after soaking/pressing in the cell), soaked with aqueous electrolyte solutions. The electrolyte solutions were prepared in Milli-Q water with varied  $Li_2SO_4$  to  $ZnSO_4$  concentrations, ranging from pure 0 M  $Li_2SO_4$  – 2 M  $ZnSO_4$  to 1.75 M  $Li_2SO_4$  – 0.25 M  $ZnSO_4$ . For the GITT analysis, 3-min 0.3 C (50 mA g<sup>-1</sup>) current pulse and 3 h rest steps were employed. The  $D_{Li+/H+}$  were calculated by applying the following equation:

$$D = \frac{4}{\pi \tau} \left( \frac{mV}{MS} \right)^2 \left( \frac{\Delta E_s}{\Delta E_t} \right)^2 \quad (2)$$

Here, where  $\tau$  is the pulse length (180 s),  $m$  is the mass of  $LiMn_2O_4$  in the electrode,  $V$  is the molar volume (obtained from the crystal structure),  $M$  is the molar mass of  $LiMn_2O_4$  and  $S$  is the electrode-electrolyte contact area. The change in steady-state voltage over the previous step and the voltage change due to the current pulse are represented by  $\Delta E_s$  and  $\Delta E_t$ , respectively. The above equation can be applied only when the voltage varies linearly with the square root of time, which was confirmed for each step.<sup>[37]</sup>

*Operando* XRD was conducted on a PANalytical Empyrean I diffractometer in Bragg–Brentano geometry using Co  $K\alpha 1$  radiation ( $\lambda = 1.788965 \text{ \AA}$ ) and a Pixel detector with a Ni  $K\beta$  filter. The diffraction data were collected in the reflection mode from 5° to 60° ( $\theta$ ) with a collection time of 15 min. The field-emission scanning electron microscopy (FE-SEM) images were obtained with an FEI Nova NanoSEM 230 equipped with energy-dispersive X-ray spectroscopy (EDX) attachment. Prior to the SEM-EDX analysis, the electrochemically cycled electrodes were extensively washed with Milli-Q water to remove any electrolyte salt. The electrodes were subsequently washed with ethanol and dried under a vacuum. A thin layer of gold (Au; 5 nm) was sputtered on the samples to avoid sample “charging” or electron accumulation on the surface under the incident electron beam.

For synchrotron X-ray diffraction, cycled electrodes ( $\approx 20 \text{ mg cm}^{-2}$  active loading) were recovered in the discharged state and washed with water. Subsequently, the electrodes were washed with 1 M  $ZnSO_4$ – $H_2O$  solution to remove the  $H^+$  intercalation byproduct  $Zn_4SO_4(OH)_6 \cdot nH_2O$ . Finally, the electrodes were again washed with water and ethanol and extensively dried under vacuum. Samples were packed into 0.3 mm quartz capillaries and mounted on the Powder Diffraction Beamline at the Australian synchrotron. Data were collected for 300 seconds, over 2 positions of the Mythen detector, using a wavelength of  $\lambda = 0.77534$  (1 Å, determined us-

ing a  $LaB_6$  660b standard reference material (SRM). Rietveld refinements were performed using GSAS-II, and the typical approach involved refinement of the background, scale factor (or phase fractions), lattice parameter, zero offset, peak shape parameters, and finally, the atomic parameters such as atomic displacements of Mn and O and the position of O in the spinel  $LiMn_2O_4$  structural model. For the comparative study, the number of refinable parameters and approach were kept as consistent as possible.

The Vienna ab initio simulation package (VASP)<sup>[38,39]</sup> was used to carry out spin-polarized DFT calculations, with the core electrons being modeled using the projector augmented wave (PAW)<sup>[40]</sup> potentials. The plane-wave basis set was expanded up to a kinetic energy cut-off of 520 eV, and sampled the irreducible Brillouin zone using a  $\Gamma$ -centred  $k$ -mesh with a density of 32 to 48  $k$ -points per Å.<sup>[41]</sup> The lattice parameters, lattice shape, and ionic positions of all structures were relaxed till the total energies and atomic forces converged to 10<sup>-5</sup> eV and |0.03| eV Å<sup>-1</sup>, respectively. The magnetic moments of Mn were initialized assuming a ferromagnetic, high-spin ordering and considering a random distribution of +3 and +4 oxidation states, depending on Li, Zn, or H content. The electronic exchange and correlation were described using the strongly constrained and appropriately normed (SCAN)<sup>[42]</sup> functional, with a Hubbard  $U$  correction of 2.7 eV added on all Mn atoms.<sup>[43–45]</sup>

The  $LiMn_2O_4$  cubic spinel (collection code: 11 273) and  $ZnMn_2O_4$  tetragonal spinel structures (collection code: 15 305) were obtained from the inorganic crystal structure database<sup>[46]</sup> as templates, and the pymatgen<sup>[47]</sup> package was used to enumerate the symmetrically distinct Li-vacancy, Zn-vacancy, and H-vacancy arrangements in the spinel. The cation-vacancy concentrations within the conventional (8 formula units) spinel cell were enumerated. While both cubic and tetragonal spinel templates at different  $Zn_xMn_2O_4$  and  $Li_xMn_2O_4$  compositions were considered, only the cubic spinel template was considered for  $H_xMn_2O_4$  compositions. For the  $ZnMn_2O_4$  composition, cubic spinel was obtained upon DFT structure relaxation irrespective of whether the cubic or the tetragonal spinel structure was used as the template. For the  $H_xMn_2O_4$  systems, H atoms were initialized in both the empty tetrahedral (8a) and octahedral (16c) sites of the cubic spinel- $Mn_2O_4$  structure,<sup>[48]</sup> and H was found to prefer the tetrahedral sites. Also, a three-step relaxation procedure devised in our previous work for the structural relaxation of  $H_xMn_2O_4$  structures was utilized.<sup>[49]</sup>

To calculate the average intercalation voltages for Li, Zn, and H (de)intercalation in  $Mn_2O_4$ , the following equations were used.<sup>[50]</sup> Note that the Gibbs energy of all compositions was approximated to their corresponding internal energy, as calculated by DFT at 0 K, that is, ( $G \approx E$ ), and we ignored any  $p - V$  contributions.  $F$  is Faraday's constant.  $E_{Li}$ ,  $E_{Zn}$ , and  $E_H$  are referenced to their respective ground states under ambient conditions, that is, body-centered-cubic Li, hexagonal-close-packed Zn, and H<sub>2</sub> gas. Once the voltages were calculated with respect to Li (for  $Li_xMn_2O_4$ ) and H (for  $H_xMn_2O_4$ ), the differences in the standard reduction potentials between  $Li^+/Li$  (−3.04 V vs SHE),  $H^+/H_2$  (0.0 V vs SHE), and  $Zn^{2+}/Zn$  (−0.77 V vs SHE) were used to re-scale the voltages with respect to the  $Zn^{2+}/Zn$  reference.

I) For  $Li_xMn_2O_4$ :

$$\Delta V = - \frac{E_{Li_{x+\Delta x}Mn_2O_4} - E_{Li_xMn_2O_4} - \Delta x E_{Li}}{1 \cdot \Delta x \cdot F} \quad (3)$$

II) For  $Zn_xMn_2O_4$ :

$$\Delta V = - \frac{E_{Zn_{x+\Delta x}Mn_2O_4} - E_{Zn_xMn_2O_4} - \Delta x E_{Zn}}{2 \cdot \Delta x \cdot F} \quad (4)$$

III) For  $H_xMn_2O_4$ :

$$\Delta V = - \frac{E_{H_{x+\Delta x}Mn_2O_4} - E_{H_xMn_2O_4} - \Delta x E_H}{1 \cdot \Delta x \cdot F} \quad (5)$$

## Supporting Information

Supporting Information is available from the Wiley Online Library or from the author.

## Acknowledgements

D.K. acknowledges UNSW's support through the faculty start-up grant. N.S. acknowledges the financial support received through the Australian Government's ARC Future Fellowship funding (FT200100707). The authors also acknowledge the Mark Wainwright Analytical Center at UNSW for access and support with the extensive *operando* XRD study presented here.

Open access publishing facilitated by University of New South Wales, as part of the Wiley - University of New South Wales agreement via the Council of Australian University Librarians.

## Conflict of Interest

The authors declare no conflict of interest.

## Author Contributions

D.K. conceived the project and designed the experiments with contributions from A.B. and G.S.G. A.B. and D.K. performed the experimental work and analyzed the data with help from U.M. A.B., S.S., and G.S.G. carried out the computational investigation and the data analysis. N.S. performed the synchrotron data analysis. D.K. wrote the manuscript with contributions from all authors.

## Data Availability Statement

The data that support the findings of this study are available from the corresponding author upon reasonable request.

## Keywords

aqueous battery, charge storage mechanism, inhibition of H<sup>+</sup> intercalation, *operando* X-ray diffraction, stabilizing output voltage decay

Received: March 5, 2024

Revised: April 1, 2024

Published online:

- [1] B. Turley, A. Cantor, K. Berry, S. Knuth, D. Mulvaney, N. Vineyard, *Energy Res. Soc. Sci.* **2022**, *90*, 102583.
- [2] A. G. Olabi, C. Onumaegbu, T. Wilberforce, M. Ramadan, M. A. Abdelkareem, A. H. Al-Alami, *Energy* **2021**, *214*, 118987.
- [3] Z. Yang, J. Zhang, M. C. W. Kintner-Meyer, X. Lu, D. Choi, J. P. Lemmon, J. Liu, *Chem. Rev.* **2011**, *111*, 3577.
- [4] P. Canepa, G. Sai Gautam, D. C. Hannah, R. Malik, M. Liu, K. G. Gallagher, K. A. Persson, G. Ceder, *Chem. Rev.* **2017**, *117*, 4287.
- [5] V. Mathew, B. Sambandam, S. Kim, S. Kim, S. Park, S. Lee, M. H. Alfaruqi, V. Soundharajan, S. Islam, D. Y. Putro, J. Y. Hwang, Y. K. Sun, J. Kim, *ACS Energy Lett.* **2020**, *5*, 2376.
- [6] X. Jia, C. Liu, Z. G. Neale, J. Yang, G. Cao, *Chem. Rev.* **2020**, *120*, 7795.
- [7] T. Xiong, Z. G. Yu, H. Wu, Y. Du, Q. Xie, J. Chen, Y. Zhang, S. J. Pennycook, W. S. V. Lee, J. Xue, *Adv. Energy Mater.* **2019**, *9*, 1803815.
- [8] G. Yuan, J. Bai, T. N. L. Doan, P. Chen, *Mater. Lett.* **2014**, *137*, 311.
- [9] Y. Shang, D. Kundu, *Joule* **2023**, *7*, 244.
- [10] V. Verma, S. Kumar, W. Manalastas, M. Srinivasan, *ACS Energy Lett.* **2021**, *6*, 1773.
- [11] M. J. Park, H. Yaghoobnejad Asl, A. Manthiram, *ACS Energy Lett.* **2020**, *5*, 2367.
- [12] P. Oberholzer, E. Tervoort, A. Bouzid, A. Pasquarello, D. Kundu, *ACS Appl. Mater. Interfaces* **2019**, *11*, 674.
- [13] C. Li, S. Jin, L. A. Archer, L. F. Nazar, *Joule* **2022**, *6*, 1733.
- [14] X. Liu, H. Euchner, M. Zarrabeitia, X. Gao, G. A. Elia, A. Groß, S. Passerini, *ACS Energy Lett.* **2020**, *5*, 2979.
- [15] D. Chen, M. Lu, D. Cai, H. Yang, W. Han, *J. Energy Chem.* **2021**, *54*, 712.
- [16] H. Pan, Y. Shao, P. Yan, Y. Cheng, K. S. Han, Z. Nie, C. Wang, J. Yang, X. Li, P. Bhattacharya, K. T. Mueller, J. Liu, *Nat. Energy* **2016**, *1*, 16039.
- [17] Y. Li, S. Wang, J. R. Salvador, J. Wu, B. Liu, W. Yang, J. Yang, W. Zhang, J. Liu, J. Yang, *Chem. Mater.* **2019**, *31*, 2036.
- [18] F. Wang, L. E. Blanc, Q. Li, A. Faraone, X. Ji, H. H. Chen-Mayer, R. L. Paul, J. A. Dura, E. Hu, K. Xu, L. F. Nazar, C. Wang, *Adv. Energy Mater.* **2021**, *11*, 2102016.
- [19] Y. Yuan, R. Sharpe, K. He, C. Li, M. T. Saray, T. Liu, W. Yao, M. Cheng, H. Jin, S. Wang, K. Amine, R. Shahbazian-Yassar, M. S. Islam, J. Lu, *Nat. Sustain.* **2022**, *5*, 890.
- [20] C. Li, R. Kingsbury, L. Zhou, A. Shyamsunder, K. A. Persson, L. F. Nazar, *ACS Energy Lett.* **2022**, *7*, 533.
- [21] C. Li, R. Kingsbury, A. S. Thind, A. Shyamsunder, T. T. Fister, R. F. Kliewer, K. A. Persson, L. F. Nazar, *Nat. Commun.* **2023**, *14*, 3067.
- [22] L. Zhang, I. A. Rodríguez-Pérez, H. Jiang, C. Zhang, D. P. Leonard, Q. Guo, W. Wang, S. Han, L. Wang, X. Ji, *Adv. Funct. Mater.* **2019**, *29*, 1902653.
- [23] F. Wang, O. Borodin, T. Gao, X. Fan, W. Sun, F. Han, A. Faraone, J. A. Dura, K. Xu, C. Wang, *Nat. Mater.* **2018**, *17*, 543.
- [24] W. Yu, Y. Liu, L. Liu, X. Yang, Y. Han, P. Tan, *J. Energy Storage* **2022**, *45*, 103744.
- [25] J. Zhi, A. Z. Yazdi, G. Valappil, J. Haime, P. Chen, *Sci. Adv.* **2017**, *3*, e1701010.
- [26] J. Yan, J. Wang, H. Liu, Z. Bakenov, D. Gosselink, P. Chen, *J. Power Sources* **2012**, *216*, 222.
- [27] A. Bhandari, J. Bhattacharya, *J. Electrochem. Soc.* **2017**, *164*, A106.
- [28] X. Zhang, X. Lan, Y. Feng, X. Wang, S. Kong, Z. Xu, Z. Ma, W. Gong, Y. Yao, Q. Li, *Adv. Mater. Inter.* **2023**, *10*, 2202035.
- [29] P. Hohenberg, W. Kohn, *Phys. Rev.* **1964**, *136*, B864.
- [30] W. Kohn, L. J. Sham, *Phys. Rev.* **1965**, *140*, A1133.
- [31] O. Y. Long, G. Sai Gautam, E. A. Carter, *Phys. Chem. Chem. Phys.* **2021**, *23*, 24726.
- [32] Z. Rong, R. Malik, P. Canepa, G. Sai Gautam, M. Liu, A. Jain, K. Persson, G. Ceder, *Chem. Mater.* **2015**, *27*, 6016.
- [33] R. D. Bayliss, B. Key, G. Sai Gautam, P. Canepa, B. J. Kwon, S. H. Lapidus, F. Dogan, A. A. Adil, A. S. Lipton, P. J. Baker, G. Ceder, J. T. Vaughan, J. Cabana, *Chem. Mater.* **2020**, *32*, 663.
- [34] R. Malik, F. Zhou, G. Ceder, *Nat. Mater.* **2011**, *10*, 587.
- [35] G. S. Gautam, P. Canepa, in *Energy and Environmental Series* (Ed: M. Fichtner), Royal Society of Chemistry, Cambridge **2019**, pp. 79–113.
- [36] C. Huang, Q. Wang, G. Tian, D. Zhang, *Mater. Today Phys.* **2021**, *21*, 100518.
- [37] J. Kim, S. Park, S. Hwang, W.-S. Yoon, *J. Electrochem. Sci. Technol.* **2022**, *13*, 19.
- [38] G. Kresse, J. Hafner, *Phys. Rev. B* **1993**, *47*, 558.
- [39] G. Kresse, J. Furthmüller, *Phys. Rev. B* **1996**, *54*, 11169.
- [40] G. Kresse, D. Joubert, *Phys. Rev. B* **1999**, *59*, 1758.
- [41] D. B. Tekliye, A. Kumar, X. Weihang, T. D. Mercy, P. Canepa, G. Sai Gautam, *Chem. Mater.* **2022**, *34*, 10133.
- [42] J. Sun, A. Ruzsinszky, J. Perdew, *Phys. Rev. Lett.* **2015**, *115*, 036402.
- [43] G. Sai Gautam, E. A. Carter, *Phys. Rev. Mater.* **2018**, *2*, 095401.

- [44] V. I. Anisimov, J. Zaanen, O. K. Andersen, *Phys. Rev. B* **1991**, *44*, 943.
- [45] S. Dudarev, G. Botton, *Phys. Rev. B* **1998**, *57*, 1505.
- [46] M. Hellenbrandt, *Crystallogr. Rev.* **2004**, *10*, 17.
- [47] S. P. Ong, W. D. Richards, A. Jain, G. Hautier, M. Kocher, S. Cholia, D. Gunter, V. L. Chevrier, K. A. Persson, G. Ceder, *Comput. Mater. Sci.* **2013**, *68*, 314.
- [48] G. Sai Gautam, P. Canepa, A. Urban, S. H. Bo, G. Ceder, *Chem. Mater.* **2017**, *29*, 7918.
- [49] G. Sai Gautam, P. Canepa, W. D. Richards, R. Malik, G. Ceder, *Nano Lett.* **2016**, *16*, 2426.
- [50] M. Aydinol, A. Kohan, G. Ceder, K. Cho, J. Joannopoulos, *Phys. Rev. B* **1997**, *56*, 1354.